

=enter title here=

=list all authors here=

=number= =Affiliation Address=

4 Key Points:

- 5** • enter point 1 here
6 • enter point 2 here
7 • enter point 3 here

Corresponding author: =name=, =email address=

8 **Abstract**
 9 enter abstract here

10 **1 Introduction**

11 Slow slip events are a new feature discovered in the last two decades in many sub-
 12 duction zones thanks to recordings of the displacement of Earth's surface by dense Global
 13 Navigation Satellite System (GNSS) networks. As with ordinary earthquakes, slow slip
 14 events are caused by slip on a fault, such as the plate boundary between a tectonic plate
 15 subducting under another tectonic plate. However, they take a much longer time (sev-
 16 eral days to several years) to happen relative to ordinary earthquakes, and they have a
 17 relatively short recurrence time (months to years), compared to the recurrence time of
 18 regular earthquakes (up to several hundreds of years), allowing scientists to observe and
 19 study many complete event cycles, which is typically not possible to explore with tra-
 20 ditional earthquake catalogs (Beroza & Ide, 2011). A slow slip event on the plate bound-
 21 ary is inferred to happen when there is a reversal of the direction of motion at GNSS sta-
 22 tions, compared to the secular interseismic motion. Slow slip events have been observed
 23 in many subduction zones, such as Cascadia, Nankai (southwest Japan), Alaska, Costa
 24 Rica, Mexico, and New Zealand (Audet & Kim, 2016; Beroza & Ide, 2011).

25 In many places, tectonic tremor are also observed in relation to slow slip. Tremor
 26 is a long (several seconds to many minutes), low amplitude seismic signal, with emer-
 27 gent onsets, and an absence of clear impulsive phases. Tectonic tremor have been explained
 28 as a swarm of small, low-frequency earthquakes (LFEs) (Shelly, Beroza, & Ide, 2007),
 29 that is small magnitude earthquakes ($M \sim 1$), for which frequency content (1-10 Hz) is
 30 lower than for ordinary earthquakes (up to 20 Hz). In subduction zones such as Nankai
 31 and Cascadia, tectonic tremor observations are spatially and temporally correlated with
 32 slow slip observations (Obara, 2002; Rogers & Dragert, 2003). Due to this correlation,
 33 these paired phenomena have been called Episodic Tremor and Slip (ETS). However, this
 34 is not always the case. For instance, in northern New Zealand, tremor are more challeng-
 35 ing to detect, and seem to be located downdip of the slow slip on the plate boundary.

36 In Cascadia and Guerrero, Mexico, tremor has been used as a proxy to observe slow
 37 slip events that are not directly detectable in the GNSS data. For instance, Aguiar, Mel-
 38 bourne, and Scrivner (2009) computed the GPS-estimated moment release for 23 ETS
 39 events in Cascadia between 1997 and 2008. Simultaneously, they computed the cumu-
 40 lative number of hours of tectonic tremor recorded for each event. They observed a lin-
 41 ear relationship between moment release and number of hours of tremor for ETS events
 42 of moment magnitude 6.3 to 6.8. For all these events, at least 50 hours of tectonic tremor
 43 where observed simultaneously with the GPS deformation. However, many smaller bursts
 44 of tremor of duration 1 to 50 hours were also observed in between the big ETS events.
 45 Based on the relationship between slow slip moment and number of hours of tremor, Aguiar
 46 et al. (2009) suggested that smaller slow slip events of magnitude 5-6 may occur sim-
 47 taneously with the tremor bursts without being detectable in the GPS data.

48 Frank (2016) transformed the GPS time series into daily increments of surface mo-
 49 tion by computing the first order differentiation of the time series. He then discarded
 50 the daily increments observed during known big slow slip events, and focused on the inter-
 51 events period. He divided the daily increments into two groups: the first group contains
 52 days when slow seismicity (tectonic tremor and LFEs) is detected, the second group con-
 53 tains days when the numbers of LFEs (for Guerrero) or tremor (for Cascadia) is lower
 54 than a threshold. He then stacked separately the two groups of daily increments and ob-
 55 served a cumulative displacement in the northern direction (for Guerrero) and the east-
 56 ern direction (for Cascadia) corresponding to the loading period when few tremor or LFEs
 57 are observed and the surface deformation corresponds to the secular plate motion. He
 58 also observed a cumulative displacement in the southern direction (for Guerrero) and
 59 the western direction (for Cascadia) corresponding to the release period when tremor

60 and LFEs are observed. This reverse displacement corresponds to smaller slow slip events
61 not directly observable in the GPS data.

62 However, in other subduction zones such as New Zealand, there is no clear rela-
63 tionship between tremor and slow slip occurrence and these methods cannot be applied.
64 We thus need other methods to be able to better detect and quantify slow slip.

65 Wavelets methods such as the Discrete Wavelet Transform (DWT) are mathemat-
66 ical tools for analyzing time series simultaneously in the time and the frequency domain
67 by observing how weighted averages of a time series vary from one averaging period to
68 the next. Wavelet methods have been widely used for geophysical applications (Kumar
69 & Foufoula-Georgiou, 1997). However, few studies have used wavelet methods to ana-
70 lyze recordings of slow slip, and their scope was limited to the detection of the bigger
71 (magnitude 6-7) short-term (a few weeks) events.

72 Alba, Weldon, Livelybrooks, and Schmidt (2019) used hourly water level records
73 from four tide gauges in the Juan de Fuca Straight and the Puget Sound to determine
74 vertical displacements, uplift rates between ETS events, and net uplift rates between 1996
75 and 2011. The noise in the tide gauges data is associated with tides, and ocean and at-
76 mospheric noise on multiple timescales (a few days for storms to decades for oscillations
77 between ocean basins), and is assumed to be coherent between each of the four tidal gauges
78 studied. On the contrary, the uplift due to ETS events should be different at each tidal
79 gauge. They first removed the tides using NOAA hourly harmonic tidal predictions. They
80 then removed the residual noise using a method based on the DWT. More precisely, the
81 authors applied a DWT to each of the four sites studied, and to the average of the four
82 sites. Then, for each level of the DWT decomposition, they carried out a linear regres-
83 sion between the detail for one site and the detail for the average of the four sites. This
84 process gives a coefficient for each level and for each site. They then constructed a noise
85 signal for each site by multiplying the coefficient from the linear regression by the de-
86 tail of the average over the four sites, and summing for all levels. The noise signal thus
87 obtained was then removed from the time series. They then stacked multiple events to
88 obtain an average event uplift rate, aligning the 12 ETS events using exact timing from
89 GPS data. A difference in uplift between the two tidal gauges at Port Angeles and Port
90 Townsend was then clearly seen in the stacked time series. Finally, the authors removed
91 the long-term uplift rate and the long-term sea level rise to obtain an average inter-event
92 uplift rate. They found that the inter-event deformation at a site is equal and opposite
93 to the deformation during an ETS event, suggesting that ETS events are, on average,
94 releasing the strain accumulated between ETS events.

95 Szeliga, Melbourne, Santillan, and Miller (2008) determined the timing and the
96 amplitude of 34 slow slip events throughout the Cascadia subduction zone between 1997
97 and 2005. They stabilized the GPS time series using a reference set of stations from sta-
98 ble North America. They then modelled the GPS time series by the sum of a linear trend,
99 annual and biannual sinusoids representing seasonal effects, and Heaviside step functions
100 corresponding to earthquakes and hardware upgrades. The linear system was then solved
101 using a weighted QR decomposition. Finally, they applied a Gaussian wavelet transform
102 to the residual time series to get the exact timing of the slow slip at each GPS station.
103 The succeeding wavelet basis functions are increasingly sensitive to temporal localiza-
104 tion of a given signal, and the onset of faulting appears on the wavelet spectrum as an
105 amplitude spike present over all frequencies. The offset for each slow slip event was then
106 used to invert for the slow slip at depth by assuming a thrust fault slip at each subfault
107 of the plate boundary. An equivalent moment magnitude was thus obtained.

108 Finally, instead of using wavelets in the time domain, Ohtani, McGuire, and Segall
109 (2010) used 2D wavelet functions in the spatial domain to detect slow slip events. They
110 designed the Network Stain Filter (NSF) to detect transient deformation signals from
111 large-scale geodetic arrays. Contrary to their previous work on the Network Inversion
112 Filter (NIF), there is no need to specify potential sources of deformation. They mod-
113 elled the position of the GPS station by the sum of the secular velocity, a spatially co-
114 herent field, site-specific noise, reference frame errors, and observation errors. The spa-

115 tial displacement field is modeled by the sum of basis wavelets (the Deslauriers-Dubuc
 116 wavelet of degree 3) with time-varying weights. The transient is considered to be nearly
 117 steady-state, so that it has spatial weights for the displacement and the velocity, but the
 118 acceleration is modeled by a random walk with a time-varying variance. All the time varying
 119 coefficients are estimated using Kalman filtering, and the optimization problem is
 120 regularized with the spatial sum of the transient strain rate field. Their method has been
 121 successfully used to detect a transient event in the Boso peninsula, Japan, and a slow
 122 slip event in the Alaska subduction zone (Wei, McGuire, & Richardson, 2012).

123 In this study, we use wavelet methods to analyze GPS and seismic recordings of
 124 slow slip events in Cascadia. Our objective is to verify that there is a good correlation
 125 between slow slip events detected with only GNSS data, and slow slip events detected
 126 with only seismic data. We thus want to demonstrate that the wavelet-based detection
 127 method can be applied to detect slow slip events that may be currently undetected with
 128 standard methods.

129 2 Data

130 We focused our study on northwest Washington State. For the GNSS data, we used
 131 the GPS time series provided by the Pacific Northwest Geodetic Array, Central Wash-
 132 ington University. These are network solutions in ITRF2008 with phase ambiguities re-
 133 solved. Solutions are computed with JPL/NASA orbits and satellite clocks. North, East,
 134 and Vertical directions are available. However, as the direction of the secular plate mo-
 135 tion is close to the East direction, we only used the East direction of the GPS time se-
 136 ries for the data analysis, as it has the best signal-to-noise ratio. The wavelet method
 137 works best with data with zero mean, and no sharp discontinuities, so we use the cleaned
 138 dataset, that is GPS times eries with linear trends, steps due to earthquakes or hard-
 139 ware upgrades, and annual and semi-annual sinusoids signals simultaneously estimated
 140 and removed following Szeliga, Melbourne, Miller, and Santillan (2004). For the seis-
 141 mic data, we used the tremor catalog from the Pacific Northwest Seismic Network (PNSN)
 142 (Wech, 2010). Tremor were detected and located using waveform envelope correlation
 143 and clustering and a centroid location is available for every given five-minute time win-
 144 dow when tremor was detected. As the catalog starts in August 2009, we only looked
 145 at GPS data recorded in 2009 or later.

146 3 Method

147 3.1 The Maximal Overlap Discrete Wavelet Transform

148 The Discrete Wavelet Transform (DWT) is an orthonormal transform that trans-
 149 forms a time series X_t ($t = 0, \dots, N - 1$) into a vector of wavelet coefficients W_i ($i = 0, \dots, N - 1$).
 150 If we denote J the level of the wavelet decomposition, and we have $N = n*2^J$, where
 151 n is some integer higher or equal to 1, the vector of wavelet coefficients can be decom-
 152 posed into J wavelet vectors W_j of lengths $\frac{N}{2}, \frac{N}{4}, \dots, \frac{N}{2^J}$, and one scaling vector V_J of
 153 length $\frac{N}{2^J}$. Each wavelet vector W_j is associated with changes on scale $\tau_j = dt2^{j-1}$, where
 154 dt is the time step of the time series, and corresponds to the filtering of the original time
 155 series with a filter with nominal frequency interval $[\frac{1}{dt2^{j+1}}, \frac{1}{dt2^j}]$. The scaling vector V_J
 156 is associated with averages in scale $\lambda_J = dt2^J$, and corresponds to the filtering of the
 157 original time series with a filter with nominal frequency interval $[0, \frac{1}{dt2^{j+1}}]$. We can also
 158 define for $j = 1, \dots, J$ the j th wavelet detail D_j , which is a vector of length N , and
 159 is associated to scale $\tau_j = dt2^{j-1}$. Similarly, we can define for $j = 1, \dots, J$ the j th
 160 wavelet smooth S_j , which is a vector of length N , and is associated to scales $\tau_{j+1} = dt2^{j+1}$
 161 and higher. Together, the details and the smooths define the multiresolution analysis (MRA)
 162 of X :

$$X = \sum_{j=1}^J D_j + S_J \quad (1)$$

The DWT present several disadvantages. First, the length of the time series must be a multiple of 2^J where J is the level of the DWT decomposition. Second, the time step of the wavelet vector W_j is $dt2^j$, which may not correspond to the time when some interesting phenomenon is visible on the original time series. Third, when we circularly shift the time series, the corresponding wavelet coefficients, details and smooths are not a circularly shifted version of the wavelet coefficients, details and smooths of the original time series. Thus, the values of the wavelet coefficients, details and smooths are strongly dependent on the time when we start experimentally gathering the data. Finally, when we filter the time series to obtain the details and smooths, we introduce a phase shift, which makes difficult to line up meaningfully the features of the MRA with the original time series.

This is why we use instead the Maximal Overlap Discrete Wavelet Transform (MODWT). The MODWT transforms the time series X_t ($t = 0, \dots, N - 1$) into J wavelet vectors \tilde{W}_j ($j = 1, \dots, J$) of length N and a scaling vector \tilde{V}_J of length N . As is the case for the DWT, each wavelet vector \tilde{W}_j is associated with changes on scale $\tau_j = dt2^{j-1}$, and corresponds to the filtering of the original time series with a filter with nominal frequency interval $[\frac{1}{dt2^{j+1}}; \frac{1}{dt2^j}]$. The scaling vector \tilde{V}_J is associated with averages in scale $\lambda_J = dt2^J$, and corresponds to the filtering of the original time series with a filter with nominal frequency interval $[0; \frac{1}{dt2^{j+1}}]$. As is the case for the DWT, we can write the MRA:

$$X = \sum_{j=1}^J \tilde{D}_j + \tilde{S}_J \quad (2)$$

The MODWT of a time series can be defined for any length N . The time step of the wavelet vectors \tilde{W}_j and the scaling vector \tilde{V}_J is equal to the time step of the original time series. When we circularly shift the time series, the corresponding wavelet vectors, scaling vector, details and smooths are shifted by the same amount. The details and smooths are associated with a zero phase filter, making it easy to line up meaningfully the features of the MRA with the original time series. The wavelet methods for time series analysis are explained in a more detailed way in Percival and Walden (2000)).

3.2 Application to synthetic data

To illustrate the wavelet transform method, we first apply the MODWT to synthetics data. As slow slip events occur in Cascadia on a regular basis, every twelve to eighteen months, we create a synthetic signal of period $T = 500$ days. To reproduce the ground displacement observed on the longitudinal component of GPS stations in Cascadia, we divide each period into two parts: In the first part of duration $T-N$, the displacement is linearly increasing and corresponds to the secular plate motion in the eastern direction; in the second part of duration N , the displacement is linearly decreasing and corresponds to a slow slip event on a reverse fault at depth triggering a ground displacement in the western direction. To see the effect of the magnitude of the slow slip event, we use different values for $N = 2, 5, 10, 20$ days. Figure 1 shows the synthetics, the details of the wavelet decomposition for levels 1 to 8, and the smooth for the four durations of a slow slip event.

The ramp-like signal is transformed through the wavelet filtering into a waveform with first a positive peak and then a negative peak. The width of the waveform increases with the scale level. For the 8th level of the wavelet decomposition, the width of the waveform is nearly as large as the time between two events. We do not show details at larger scales as the corresponding waveforms would start to merge two contiguous events to-

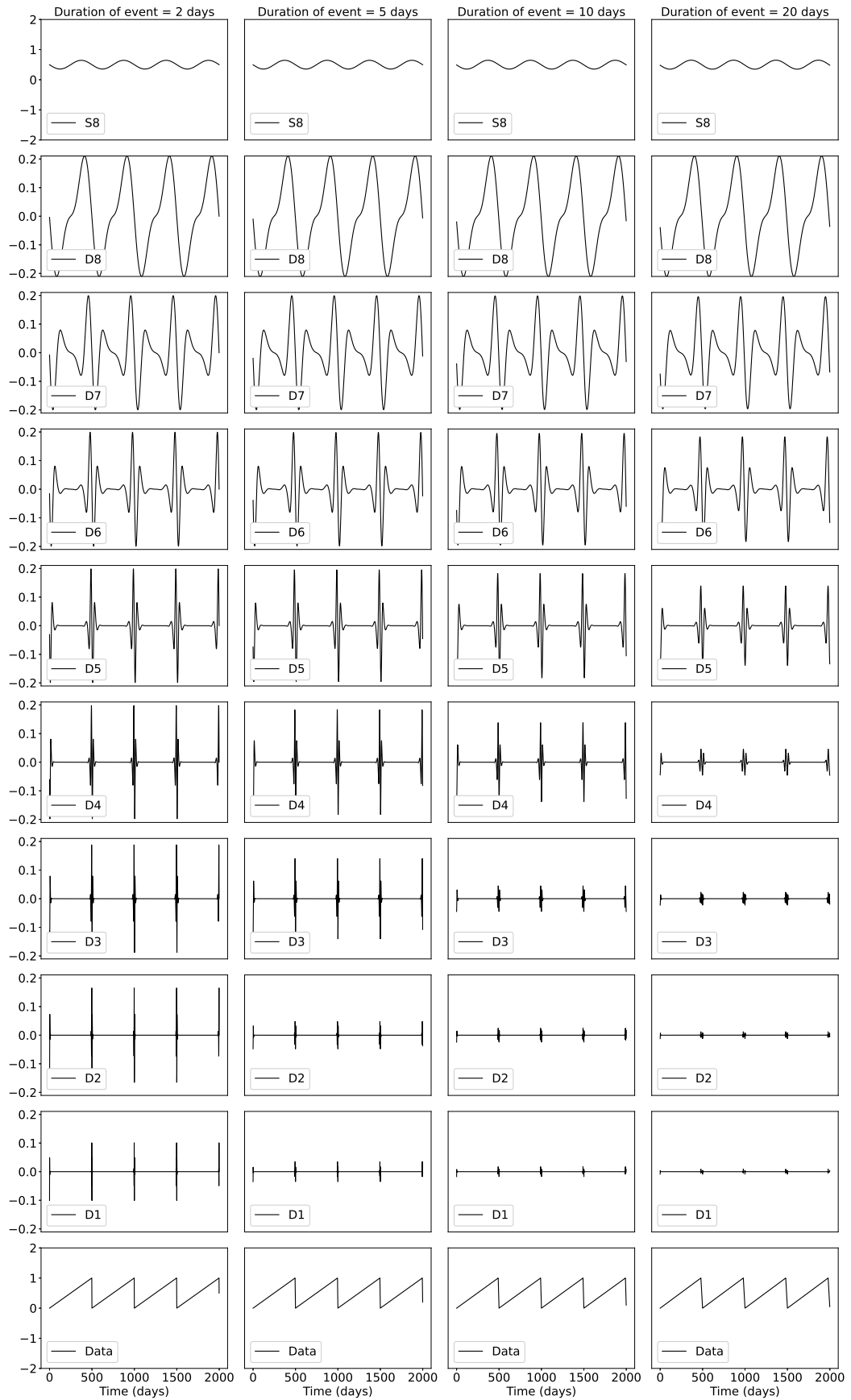


Figure 1. Details and smooth of the wavelet decomposition of a synthetics signal with period 500 days and duration of the slow slip event equal to 2 days (left), 5 days, 10 days, and 20 days (right).

209 gether, and make the wavelet decomposition less interpretable. For an event of duration
 210 2 days, the wavelet details at levels higher than 2 have a larger amplitude than the wavelet
 211 detail at level 1. For an event of duration 5 days, the wavelet details at levels higher than
 212 3 have a larger amplitude than the wavelet details at lower scales. For an event of du-
 213 ration 10 days, the wavelet details at levels higher than 5 have a larger amplitude than
 214 the wavelet details at lower scales. For an event of duration 20 days, the wavelet details
 215 at levels higher than 6 have a larger amplitude than the wavelet details at lower scales.
 216 Thus, the scale levels at which an event is being seen in the wavelet details give us an
 217 indication about the duration (and the magnitude) of the slow slip event. We expect the
 218 big slow slip events of magnitude 6-7 that lasts about 10 days to start being visible at
 219 the level 5 of the wavelet decomposition, but to not be noticeable at lower time scales.

220 3.3 MODWT of GPS and tremor data

221 The DWT and MODWT methods must be used on a continuous time series, with-
 222 out gaps in the recordings. To deal with the gaps in the GNSS recordings, we simply re-
 223 place the missing values by Gaussian noise with mean zero and standard deviation equal
 224 to the standard deviation of the whole time series. We verify how the wavelet details may
 225 be affected by looking at a GPS time series without missing values and comparing the
 226 wavelet details with and without removing some data points. Station PGC5 has recorded
 227 during 1390 days between 2009 and 2013, without any missing values. We first computed
 228 the wavelet details without missing values. Then, we removed ten neighboring missing
 229 values, replaced them by Gaussian noise, and computed the wavelet details with the re-
 230 placed values. Figure 2 shows a comparison of the two wavelet details for two different
 231 locations of the missing values. We can see that there are visible differences in the time
 232 series itself, and in the details at the smallest levels of the wavelet decomposition. How-
 233 ever, the differences between the wavelet details with and without missing values get smaller
 234 and smaller with increasing levels the details, and are barely visible for the levels we are
 235 mostly interested in (levels 6 to 8). We thus conclude that we can easily replace the miss-
 236 ing values in the GNSS time series without introducing false detections of slow slip events.

237 We then applied the wavelet filtering to real GPS data. Figure 3 shows the longi-
 238 tudinal displacement for GPS station PGC5, located in southern Vancouver Island, the
 239 details of the wavelet decomposition for levels 1 to 8, and the smooth. In the data, we
 240 can see a sharp drop in displacement whenever there is a slow slip event. For levels 5 to
 241 8, we can see in the details a positive peak followed by a negative peak whenever there
 242 is a drop in displacement in the data. We thus verify that the wavelet method can de-
 243 tect slow slip events.

244 To increase the signal-to-noise ratio and be able to better detect slow slip events,
 245 we stack the signal over several GPS stations. We choose to focus on GPS stations lo-
 246 cated close enough to the tremor zone to get a sufficiently high amplitude of the slow
 247 slip signal. We choose 16 points located on the 40 km depth contour of the plate bound-
 248 ary (model from Preston, Creager, Crosson, Brocher, and Trehu (2003)) with spacing
 249 equal 0.1 degree in latitude (red triangles on Figure 4). Then we took all the GPS sta-
 250 tions located in a 50 km radius for a given point, compute the wavelet details for the lon-
 251 gitudinal displacement of each station, and stack each detail over the GPS stations. We
 252 thus have a stacked detail for each level 1 to 8 of the wavelet decomposition.

253 To compare slow slip events detected with GPS data and slow slip events detected
 254 with seismic data, we took all the tremor epicenters located within a 50 km radius cen-
 255 tered on one of the 16 locations marked by red triangles on Figure 3. Then we computed
 256 the cumulative number of tremor within this circle. Finally, we removed a linear trend
 257 from the cumulative tremor count, and applied the wavelet transform. Figure 5 shows
 258 an example of the wavelet decomposition for the third northernmost location on Figure
 259 4 (which is closest to GPS station PGC5). Contrary to what happens for the GPS data,
 260 we see a sharp increase in the data whenever there is a tremor episode, which translates
 261 into a negative peak followed by a positive peak in the wavelet details.

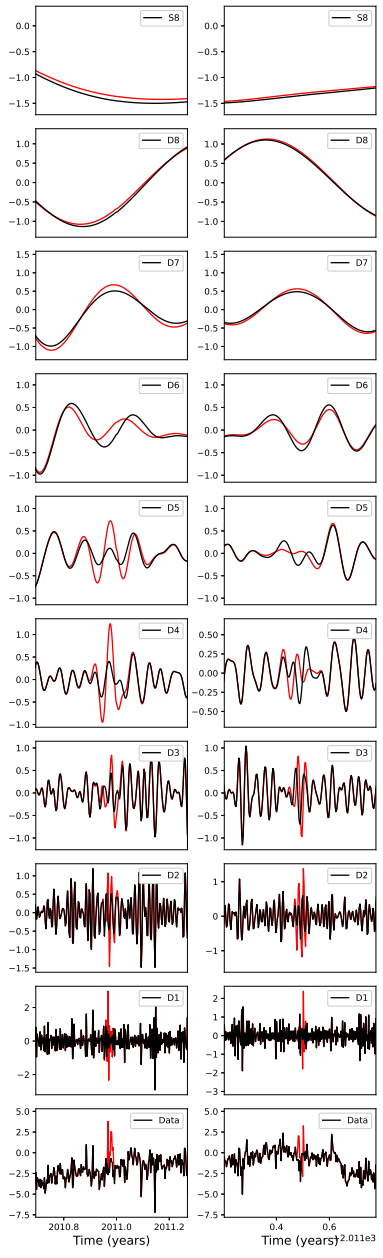


Figure 2. Bottom: Data from GPS station PGC5 without missing values (black) and with missing values replaced by Gaussian noise (red) for two locations of the missing values (left and right). Bottom to top: Corresponding eight details and smooths of the wavelet composition for the original data (black) and for the missing values replaced by Gaussian noise (red).

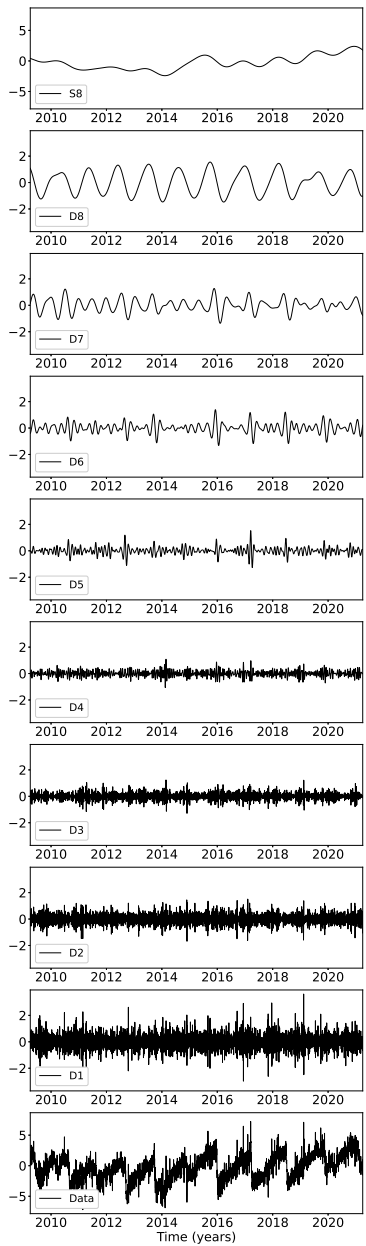


Figure 3. Details and smooth of the wavelet decomposition of the longitudinal displacement recorded at GPS station PGC5.

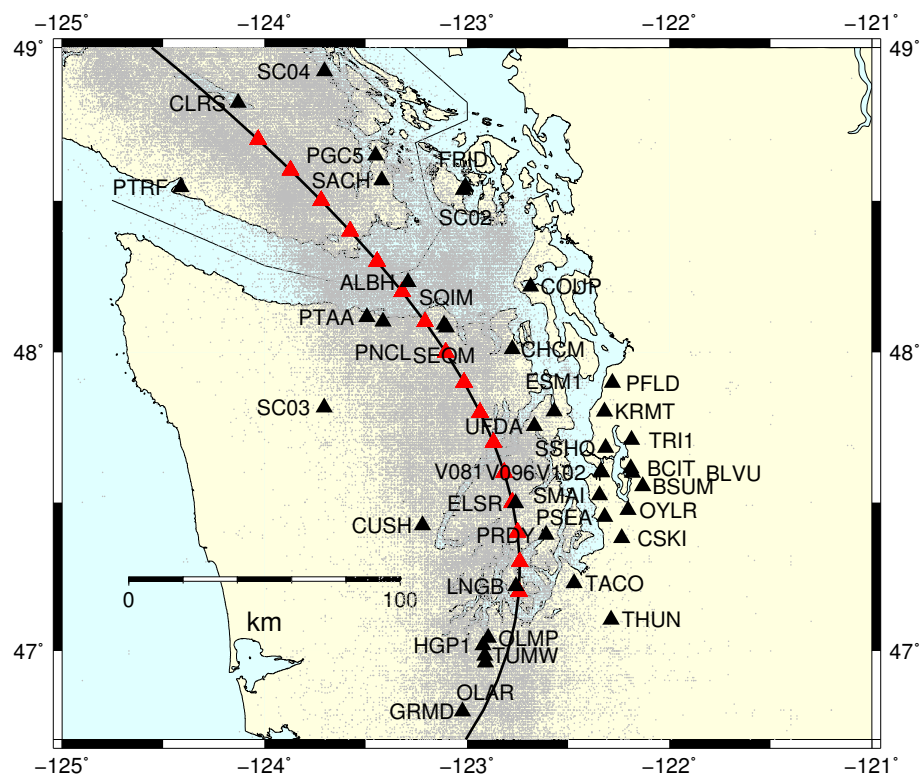


Figure 4. GPS stations used in this study (black triangles). The black line represents the 40 km depth contour of the plate boundary model by Preston et al. (2003). The red triangles are the locations where we stack the GPS data. The small grey dots are all the tremor locations from the PNSN catalog.

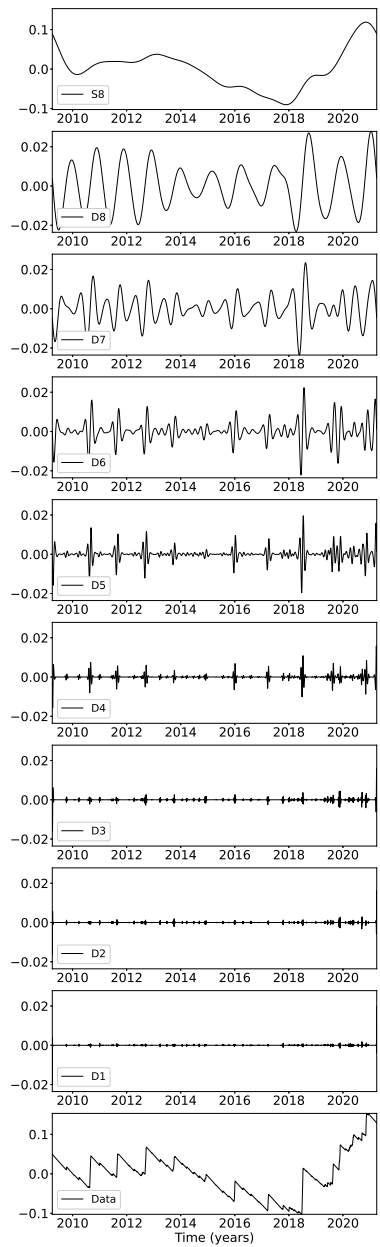


Figure 5. Details and smooth of the wavelet decomposition of the detrended cumulative tremor count around the third northernmost location on Figure 3.

262 **4 Results**

263 We stacked the 8th level detail of the wavelet decomposition of the displacement
 264 over all the GPS stations located in a 50 km radius of a given point, for the 16 locations
 265 indicated in Figure 3. The result is shown in the top panel of Figure 6, where each line
 266 represents one of the locations. To better highlight the peaks in the wavelet details, we
 267 highlighted in red the time intervals where the amplitude of the stacked detail is higher
 268 than a threshold, and in blue the time intervals where the amplitude of the stacked de-
 269 tail is lower than minus the threshold. To compare the GPS signal with the tremor sig-
 270 nal, we plotted the 8th level detail of the wavelet decomposition of the tremor count on
 271 the bottom panel of Figure 6. We used the opposite of the cumulative tremor count for
 272 the wavelet decomposition in order to be able to match positive peaks with positive peaks
 273 and negative peaks with negative peaks. Although the latitudinal extension of the events
 274 is not always the same for the GPS data and for the tremor data, we identify the same
 275 10 events in both 8th wavelet decompositions for the 8th level: Summer 2010, Summer
 276 2011, Summer 2012, Fall 2013, Summer-Fall 2014, Winter 2015-2016, Winter 2017, Spring
 277 2018, Spring-Fall 2019, and Fall 2020 - Winter 2021. We can also see the end of an 11th
 278 event in Summer 2009.

279 Figures 7 and 8 show the same comparison between the wavelet decomposition of
 280 the GPS data and the wavelet decomposition of the tremor count data for the 7th level
 281 and the 6th level respectively. For the 7th level, we see the same events as for the 8th
 282 level, both for the GPS data and the tremor count data. The wavelet decomposition is
 283 more noisy for the GPS data in the earliest part of the time series, between 2010 and
 284 2013, but it does not seem that there are more slow slip events visible in the 7th level.

285 For the 6th level detail, we see an additional event in Fall 2009 that is present both
 286 in the GPS and the tremor data. There are three small signals in the GPS data in Spring
 287 2012, Fall 2017, and Winter 2020 that are not present in the tremor data, and are prob-
 288 ably false detections. To summarize, all the 11 events present on the 7th and 8th level
 289 details of the wavelet decomposition are true detections, 12 of the 15 events present on
 290 the 6th level detail of the wavelet decomposition are true detections.

291 **5 Discussion**

292 In addition to the magnitude 6 events discussed above, Michel, Gualandi, and Avouac
 293 (2019) have also identified several magnitude 5 events using a variational Bayesian In-
 294 dependent Component Analysis (vbICA) decomposition of the signal. As we expect smaller
 295 magnitude events to be more visible at smaller time scales of the wavelet decomposi-
 296 tion (levels 4 and 5), we verify for all these events whether a signal can be seen at the same
 297 time as the time given in their catalog. Most of these magnitude 5 events are also sub-
 298 events of bigger magnitude 6 events. Table 1 summarizes for each event its number as
 299 indicated in the catalog from Michel et al. (2019), the beginning and end times as in-
 300 dicated in the catalog from Michel et al. (2019), whether it is visible at the level 4 of
 301 the wavelet decomposition, whether it is visible at the level 5 of the wavelet decompo-
 302 sition, and whether it is part of a bigger magnitude 6 event. All 10 events that are sub-
 303 event of a bigger event are visible at both levels 4 and 5. However, this may be due be-
 304 cause the bigger event is in at levels 6 to 8, and also at smaller time scales. For the 3
 305 small events that are not part of a bigger event, only one is visible at both time scales,
 306 the other two are visible either for level either for level 5 of the wavelet decomposition.
 307 Therefore, it is difficult to conclude whether the method can indeed detect events of mag-
 308 nitude 5.

309 **6 Conclusion**

310 **Acknowledgments**

311 Enter acknowledgments, including your data availability statement, here.

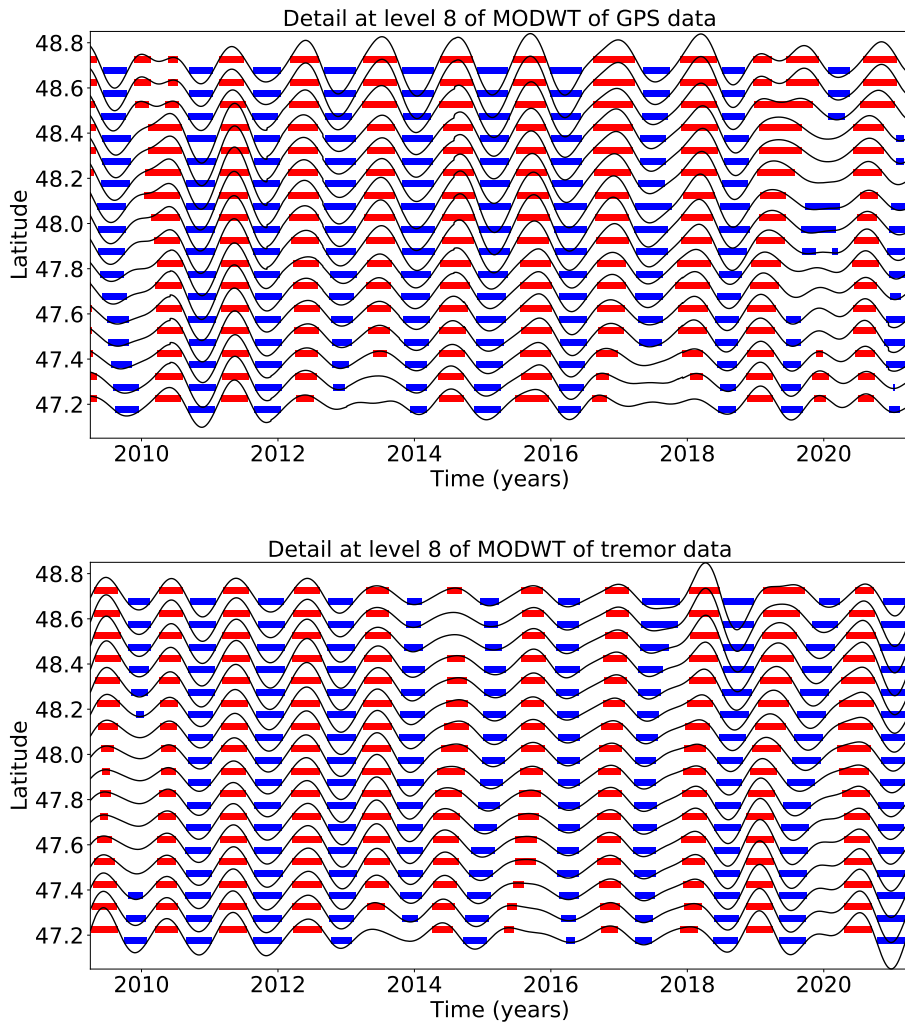


Figure 6. Top: Stacked 8th level details of the wavelet decomposition of the displacement over all the GPS stations located in a 50 km radius of a given point, for the 16 locations indicated in Figure 3. Bottom: Opposite of the 8th level detail of the cumulative tremor count in a 50 km radius of a given point for the same 16 locations.

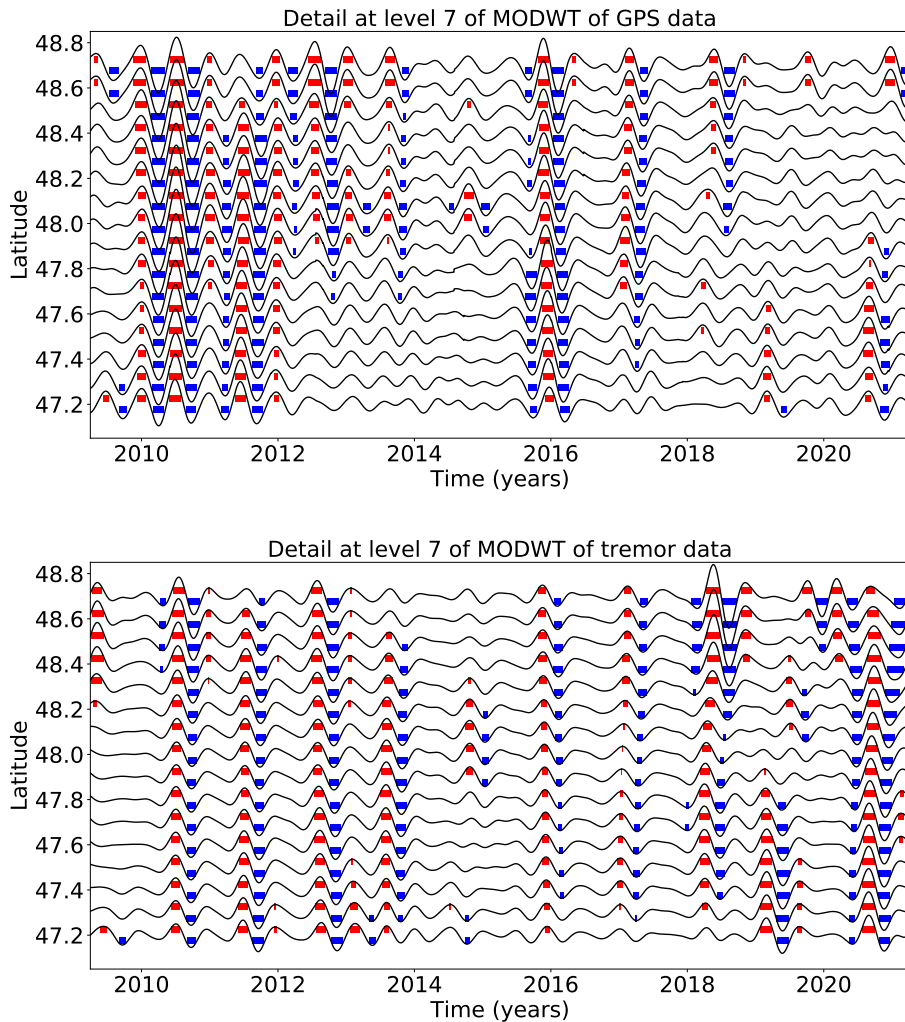


Figure 7. Top: Stacked 7th level details of the wavelet decomposition of the displacement over all the GPS stations located in a 50 km radius of a given point, for the 16 locations indicated in Figure 3. Bottom: Opposite of the 7th level detail of the cumulative tremor count in a 50 km radius of a given point for the same 16 locations.

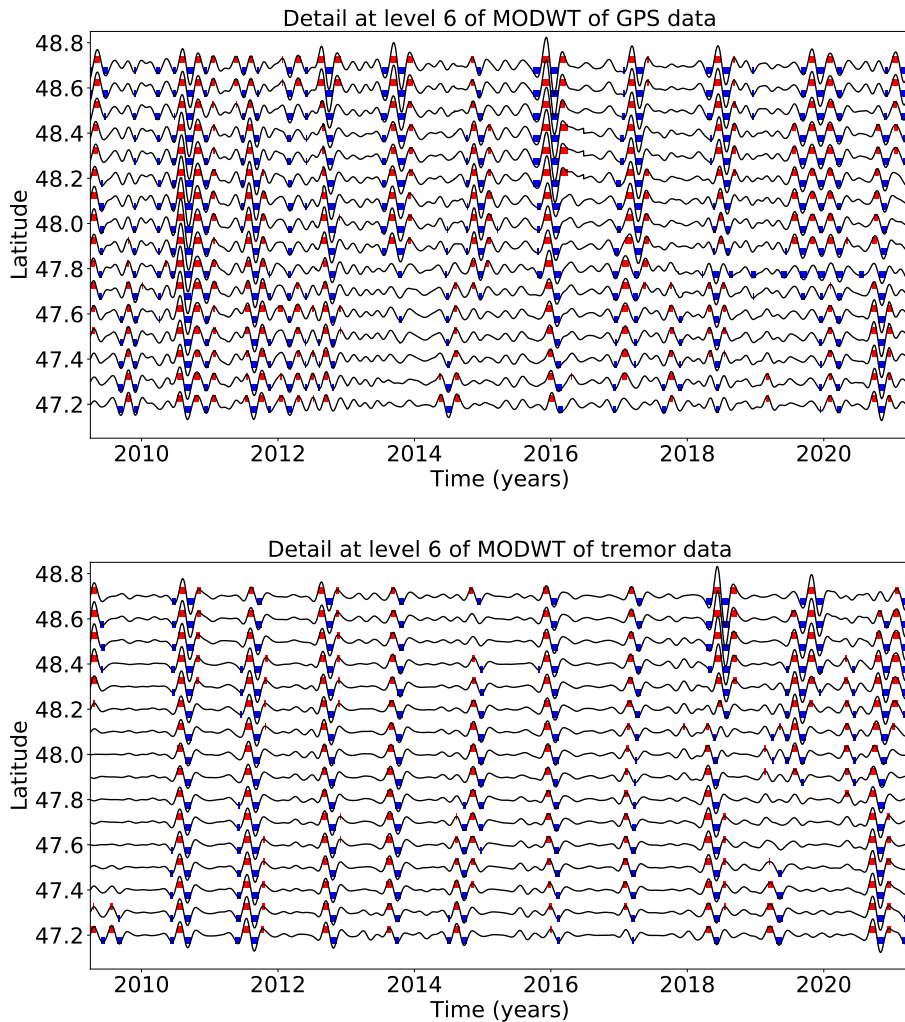


Figure 8. Top: Stacked 6th level details of the wavelet decomposition of the displacement over all the GPS stations located in a 50 km radius of a given point, for the 16 locations indicated in Figure 3. Bottom: Opposite of the 6th level detail of the cumulative tremor count in a 50 km radius of a given point for the same 16 locations.

Table 1. Magnitude 5 events from Michel et al. (2019).

Event number	Time	Visible at level 4	Visible at level 5	Sub-event of bigger event
25	2010.62-2010.67	Yes	Yes	Yes
29	2011.42-2011.45	No	Yes	No
31	2011.62-2011.68	Yes	Yes	Yes
32	2011.65-2011.68	Yes	Yes	Yes
35	2012.66-2012.72	Yes	Yes	Yes
42	2013.70-2013.78	Yes	Yes	Yes
44	2014.12-2014.20	Yes	No	No
45	2014.40-2014.48	Yes	Yes	No
49	2014.66-2014.71	Yes	Yes	Yes
52	2014.91-2014.95	Yes	Yes	Yes
57	2015.98-2016.08	Yes	Yes	Yes
60	2017.11-2017.15	Yes	Yes	Yes
61	2017.20-2017.24	Yes	Yes	Yes

312 References

- 313 Aguiar, A., Melbourne, T., & Scrivner, C. (2009). Moment release rate of Cascadia
 tremor constrained by GPS. *Journal of Geophysical Research*, *114*, B00A05.
 314
 315 Alba, S., Weldon, R. J., Livelybrooks, D., & Schmidt, D. A. (2019). Cascadia ETS
 events seen in tidal records (1980–2011). *Bulletin of the Seismological Society
 316 of America*.
 317
 318 Audet, P., & Kim, Y. (2016). Teleseismic constraints on the geological environ-
 319 ment of deep episodic slow earthquakes in subduction zone forearcs: A review.
 320 *Tectonophysics*, *670*, 1-15.
 321 Beroza, G., & Ide, S. (2011). Slow earthquakes and nonvolcanic tremor. *Annual Re-
 322 view of Earth and Planetary Sciences*, *39*, 271-296.
 323 Frank, W. (2016). Slow slip hidden in the noise: The intermittence of tectonic re-
 324 lease. *Geophysical Research Letters*, *43*, 10125-10133.
 325 Kumar, P., & Foufoula-Georgiou, E. (1997). Wavelet analysis for geophysical appli-
 326 cations. *Reviews of Geophysics*, *35*(4), 385-412.
 327 Michel, S., Gualandi, A., & Avouac, J.-P. (2019). Interseismic coupling and slow slip
 328 events on the Cascadia megathrust. *Pure and Applied Geophysics*, *176*, 3867-
 329 3891.
 330 Obara, K. (2002). Nonvolcanic deep tremor associated with subduction in southwest
 331 Japan. *Science*, *296*(5573), 1679-1681.
 332 Ohtani, R., McGuire, J., & Segall, P. (2010). Network strain filter: A new tool for
 333 monitoring and detecting transient deformation signals in GPS arrays. *Journal
 334 of Geophysical Research*, *115*, B12418.
 335 Percival, D., & Walden, A. (2000). *Wavelet Methods for Time Series Analysis*. New
 336 York, NY, USA: Cambridge University Press.
 337 Preston, L., Creager, K., Crosson, R., Brocher, T., & Trehu, A. (2003). Intraslab
 338 earthquakes: Dehydration of the Cascadia slab. *Science*, *302*, 1197-1200.
 339 Rogers, G., & Dragert, H. (2003). Tremor and slip on the Cascadia subduction zone:
 340 The chatter of silent slip. *Science*, *300*(5627), 1942-1943.
 341 Shelly, D., Beroza, G., & Ide, S. (2007). Non-volcanic tremor and low-frequency
 342 earthquake swarms. *Nature*, *446*, 305-307.
 343 Szeliga, W., Melbourne, T., Miller, M., & Santillan, V. (2004). Southern Cascadia
 344 episodic slow earthquakes. *Geophysical Research Letters*, *31*, L16602.
 345 Szeliga, W., Melbourne, T., Santillan, M., & Miller, M. (2008). GPS constraints on

- 346 34 slow slip events within the Cascadia subduction zone, 1997-2005. *Journal of*
347 *Geophysical Research*, 113, B04404.
- 348 Wech, A. (2010). Interactive tremor monitoring. *Seismological Research Letters*,
349 81(4), 664-669.
- 350 Wei, M., McGuire, J., & Richardson, E. (2012). A slow slip event in the south cen-
351 tral Alaska Subduction Zone. *Geophysical Research Letters*, 39, L15309.